Available online at www.sciencedirect.com
ScienceDirect
Trans. Nonferrous Met. Soc. China 34(2024) 3358−3371

Transactions of Nonferrous Metals Society of China
www.tnmsc.cn

Stable and reversible zinc metal anode with fluorinated graphite nanosheets surface coating

Hong CHANG[1], Zhen-ya LUO[2], Xue-ru SHI[1], Xin-xin CAO[1], Shu-quan LIANG[1]

1. Key Laboratory of Electronic Packaging and Advanced Functional Materials of Hunan Province,
School of Materials Science and Engineering, Central South University, Changsha 410083, China;
2. School of Materials Science and Engineering, Xiangtan University, Xiangtan 411105, China

Received 20 June 2024; accepted 9 August 2024

Abstract: A highly stable zinc metal anode modified with a fluorinated graphite nanosheets (FGNSs) coating was designed. The porous structure of the coating layer effectively hinders lateral mass transfer of Zn ions and suppresses dendrite growth. Moreover, the high electronegativity exhibited by fluorine atoms creates an almost superhydrophobic solid−liquid interface, thereby reducing the interaction between solvent water and the zinc substrate. Consequently, this leads to a significant inhibition of hydrogen evolution corrosion and other side reactions. The modified anode demonstrates exceptional cycling stability, as symmetric cells exhibit sustained cycling for over 1400 h at a current density of 5 mA/cm^2. Moreover, the full cells with $NH_4V_4O_{10}$ cathode exhibit an impressive capacity retention rate of 92.2% after undergoing 1000 cycles.

Key words: fluorinated graphite; hydrophobic coating; anti-corrosion; dendrite suppression; zinc metal anode

1 Introduction

Due to their high cost, lithium-ion batteries are not suitable for implementation in grid energy storage systems. As an alternative, recent reports have focused on enhancing the affordability of secondary batteries such as sodium-ion batteries [1−4], potassium-ion batteries [5,6], and zinc-ion batteries [7]. Aqueous zinc-ion batteries (AZIBs) exhibit ideal characteristics for large-scale deployment in electrochemical energy storage systems due to their safety profile and low toxicity. Moreover, these batteries offer a significant cost advantage. The utilization of a zinc metal anode, which is a fundamental component of AZIBs, enables a high theoretical capacity of 820 mA·h/g and exhibits a low redox potential of −0.76 V vs. the standard hydrogen electrode (SHE) [8−11]. A prominent issue associated with zinc metal anodes is the growth of dendrites, which can result in uneven current distribution, capacity degradation, and the potential risk of internal short circuits [10]. In addition to the problem of zinc dendrites, the zinc plating/stripping process is accompanied by parasitic reactions involving water or oxygen that can reduce cycling performance of AZIBs [12,13]. Aqueous electrolytes exhibit higher H^+ activity, leading to intense hydrogen evolution reactions (HER). The consumption of H^+ creates a localized alkaline environment on the zinc metal anode that produces inert corrosion products [14,15], which cannot act as a passivation layer to slow down further corrosion of zinc [16]. During battery operation, electrons are also consumed by HER and the generated H_2 cannot be oxidized to contribute to capacity, resulting in a decrease in battery coulombic efficiency [17].

Corresponding author: Xin-xin CAO, Tel: +86-731-88876691, E-mail: caoxinxin@csu.edu.cn
DOI: 10.1016/S1003-6326(24)66613-6

To address the challenges, a variety of strategies have been introduced to enhance the performance and stability of zinc metal anodes in AZIBs. These strategies encompass electrolyte optimization [18−20], separator functionalization [21], electrode design [22,23], and surface modification [24−29]. Among these approaches, surface coating has emerged as the most extensively investigated method due to its ease of application and consistent performance. Various materials have been employed for coating purposes, with carbon materials attracting significant attention owing to their high specific surface area, cost-effectiveness, tunable structure, and excellent stability [30]. The utilization of carbon material coatings effectively prevents direct contact between the zinc anode and the electrolyte, thereby inhibiting interfacial corrosion and parasitic reactions. Moreover, carbon materials with diverse three-dimensional structures facilitate rapid transport pathways for Zn ions, reducing polarization on the plating surface while promoting uniform Zn ions deposition. Currently, reduced graphene oxide [31,32], activated carbon [33], carbon nanotubes [34], and functional carbon blacks [35] are being used as modifying coating materials for zinc anode surfaces.

In this work, a fluorinated graphite nanosheet (FGNSs) was synthesized and firstly employed as a surface coating for zinc metal anodes. The FGNSs effectively retain the layered structure characteristic of graphite, thereby facilitating rapid transport pathways for Zn ions while simultaneously impeding lateral diffusion to prevent dendrite formation. Moreover, the exceptional hydrophobic properties resulting from the C—F covalent bond serve to isolate the highly reactive water solvent, consequently significantly suppressing hydrogen evolution corrosion and associated parasitic reactions. Consequently, zinc anodes coated with fluorinated graphite nanosheets (Zn@FGNSs) exhibit prolonged cycling lifespan and reduced polarization. This approach enables the creation of a stable Zn metal anode, ultimately enhancing the cycling stability of AZIBs.

2 Experimental

2.1 Preparation of FGNSs

The fluorinated graphene nanosheets were prepared from commercially available expanded graphite using freeze-drying and gas fluorination methods. Expanded graphite was mixed with deionized water at a mass ratio of 1:9 and stirred at 2000 r/min to create a suspension. A high-pressure homogenizer was used to process the suspension at 1000 MPa for 1 h. The homogenized suspension was freeze-dried for 12 h to obtain nano-graphene sheets. Finally, the obtained nano-graphene sheets were subjected to high-temperature fluorination under a mixed F_2/N_2 atmosphere for 9 h at 400 °C, yielding fluorinated graphene nanosheets (FGNSs).

2.2 Fabrication of Zn@FGNSs

To prepare the functional coating slurry, fluorinated graphite nanosheets (FGNSs) were mixed with polyvinylidene fluoride (PVDF) at a mass ratio of 9:1 in a sealed mixing tank using *N*-methyl-2-pyrrolidone (NMP) as the solvent, ensuring a dry environment. The mixture was then sealed and stirred for 12 h to achieve a uniformly dispersed coating slurry. Subsequently, commercial zinc foil with a thickness of 100 μm was polished using 2000-grit sandpaper as the substrate. The coating slurry was applied onto the zinc foil using a scraper and transferred to a vacuum oven for drying over 12 h, resulting in obtaining coated zinc foil (Zn@FGNSs). Furthermore, copper foil was also coated with the same slurry to create Cu@FGNSs specifically for copper-zinc half-cell testing.

2.3 Preparation of $NH_4V_4O_{10}$

Initially, 1.170 g of NH_4VO_3 (AR grade) was dissolved in deionized water at 80 °C, with continuous stirring until it completely dissolved. Subsequently, 1.891 g of oxalic acid dihydrate ($H_2C_2O_4 \cdot 2H_2O$, AR grade) was introduced to the solution and stirred for an additional 20 min. The resulting solution was then transferred to a Teflon-lined autoclave with a capacity of 50 mL and maintained at 140 °C for 48 h. Following this, the obtained product underwent thorough rinsing with deionized water and ethanol, and each was performed three times consecutively. Finally, the material was dried in a vacuum oven at 80 °C for a period of 12 h to yield $NH_4V_4O_{10}$.

2.4 Materials characterization

The phase structure was investigated by X-ray diffraction (XRD, Rigaku Mini Flex 600 diffractometer) using Cu K_α radiation (λ=1.5418 Å).

Fourier transform infrared spectroscope (FTIR) measurements were conducted using a Nicolet 6700 FTIR spectrometer (Thermo Fisher). X-ray photoelectron spectroscopy (XPS) measurements were performed on a Nexsa X-ray photoelectron spectrometer (Thermo Fisher). The microstructural morphology was collected on an optical microscope (LW750LJT), a scanning electron microscope (SEM, MIRA3, TESCAN), and a transmission electron microscope (TEM, F200X, Talos). The content of fluorine and F/C ratio were determined by a chemical method of oxygen flask combustion technique (Shanghai Institute of Organic Chemistry, China). The electrical conductivity of the samples was measured six times with the ultra-high resistance test module of four-probe workstation (Mitsubishi Chemical) to obtain the average value.

2.5 Electrode fabrication and electrochemical measurement

The modified zinc and bare zinc were punched into discs with a diameter of 15 mm to serve as anodes. Cathodes were fabricated using cathode active materials ($NH_4V_4O_{10}$), conductive carbon black (Super P), and polyvinylidene difluoride (PVDF) in a mass ratio of 7:2:1. *N*-methyl-2-pyrrolidone (NMP) was utilized as the solvent, while a stainless-steel mesh with 12 mm in diameter acted as the current collector. The cathode loading was 1.0−1.4 mg/cm^2. A glass fiber separator was employed, along with 2 mol/L $ZnSO_4$ aqueous solution as the electrolyte. The coin cells used in this study were all of the 2016-type and assembled under ambient conditions. Galvanostatic charge/discharge cycling measurements were performed using a NEWARE CT−4008 battery test system, while electrochemical impedance spectroscopy (EIS) and cyclic voltammetry (CV) tests were conducted using a CH-Instruments CHI604E electrochemical workstation.

3 Results and discussion

3.1 Characterization of FGNSs and Zn@FGNSs electrodes

The fluorinated graphene nanosheets (FGNSs) were characterized using SEM (Figs. 1(a, b)). FGNSs are composed of nanoscale sheets of a distinctive accordion-like structure. The corresponding energy-dispersive X-ray spectroscopy (EDS) image (Fig. 1(c)) demonstrates even distribution of fluorine atoms throughout the sheet material, contributing to

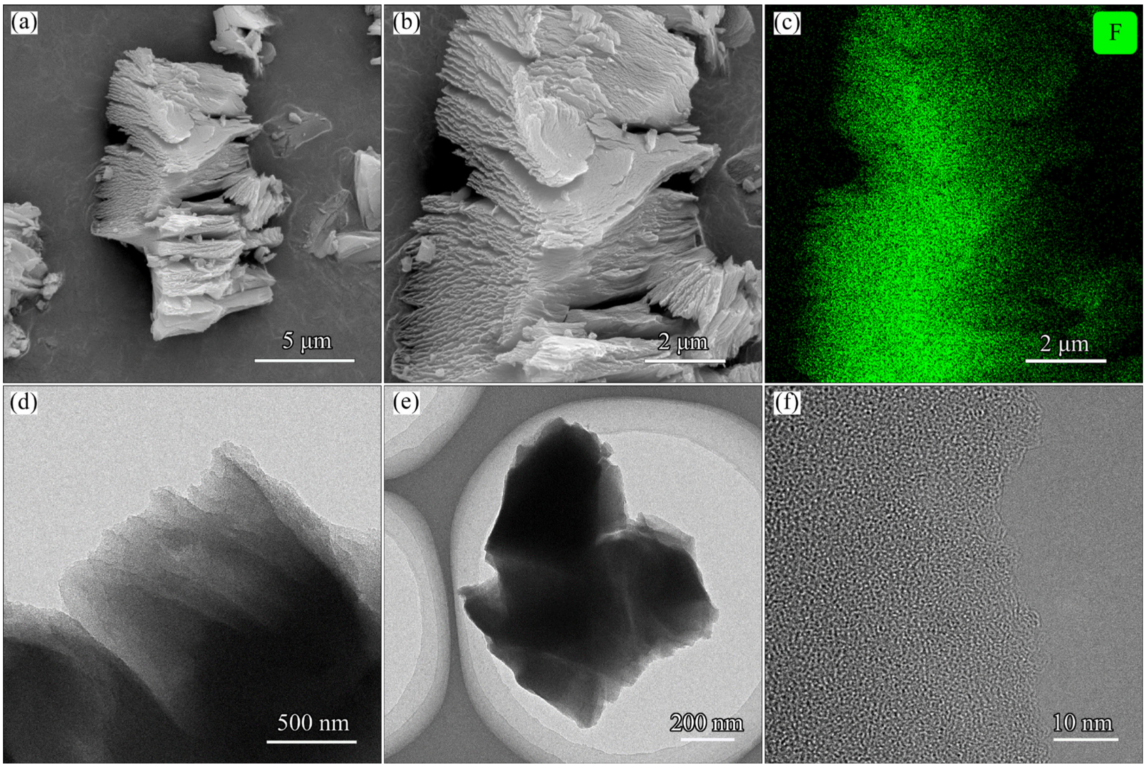

Fig. 1 Morphological characterization of FGNSs: (a, b) SEM images; (c) EDS mapping of F; (d, e) TEM images; (f) HRTEM image

the uniformity of the functional coating. Further characterization was performed using TEM, as depicted in Figs. 1(d, e), enabling a more detailed observation of the layered structure of FGNSs at a microscopic scale. The high-resolution TEM (HRTEM) image (Fig. 1(f)) does not reveal grain boundaries and exhibits a crystal structure like graphite. Additionally, the elemental composition and electrical conductivity of FGNSs are presented in Table 1. Notably, compared to graphite, FGNSs exhibit insulating properties, which facilitate direct deposition of Zn^{2+} onto the zinc substrate beneath the coating rather than on its surface.

The XRD pattern of the FGNSs sample is shown in Fig. 2(a). The diffraction peak at 2θ=26.5° corresponds to the (002) lattice plane, which aligns with the characteristic pattern of graphite. In contrast, the fluorinated FGNSs exhibit additional diffraction peaks around 14° and 41°, indicating a more intricate crystal structure and expanded interplanar spacing compared to graphite. This structural modification is expected to enhance Zn^{2+} kinetics within the coating material, thereby mitigating polarization during electroplating. The FTIR of FGNSs is shown in Fig. 2(b). The chemical structure of C—F covalent bond was determined via FTIR analysis. After fluorination, the FTIR spectrum of FGNSs exhibits a prominent peak at 1215 cm^{-1}, indicating the characteristic signature of covalent C—F bonds (Cov. C—F) [36]. Additionally, the peak at 1163 cm^{-1} corresponds to the semi-ionic C—F bond structure (S.I. C—F), while another peak at 1335 cm^{-1} represents the distinctive band associated with C—F_2 bond [36,37]. In addition to these F-related characteristic bands, strong peaks are observed at 1628 and 3430 cm^{-1}, which can be attributed to the vibrations of C═O and —OH bonds, respectively [38]. These findings suggest that fluorinated graphite retains certain bonding characteristics reminiscent of graphene oxide.

Table 1 Chemical compositions and conductivity of FGNSs

Fluorine content/wt.%	F/C ratio	Conductivity/($S\cdot m^{-1}$)
48.5	0.6	2.5×10^{-7}

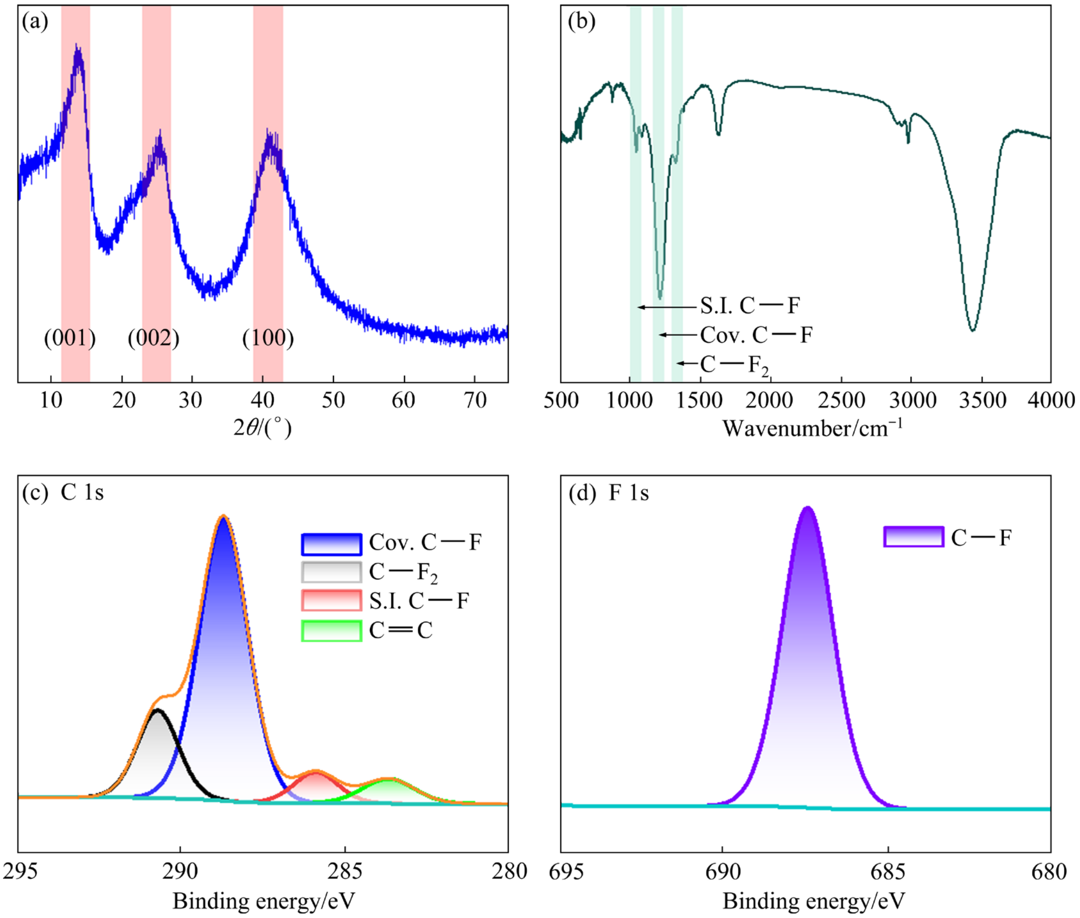

Fig. 2 XRD pattern of FGNSs (a); FTIR spectrum of FGNSs (b); high-resolution C 1s (c) and F 1s (d) XPS spectra of FGNSs

The chemical bonding properties of FGNSs were further analyzed using XPS, and the characterized chemical bond structures are consistent with those obtained from FTIR. In C 1s fine spectrum (Fig. 2(c)), photoelectron peaks can be fitted at 288.7, 285.9, 290.7, and 283.7 eV, corresponding to characteristic photoelectrons of covalent C—F bonds (Cov. C—F), semi-ionic C—F bonds (S.I. C—F), C—F_2 bonds, and C═C bonds, respectively [39]. In F 1s fine spectrum (Fig. 2(d)), clear characteristic photoelectron peaks of the F atoms in C—F bonds also appear [39]. The XPS characterization further proves that the F atoms in FGNSs are not simply adsorbed on the surface or intercalated between layers of carbon material but form stable compounds through fully bonded covalent interactions with carbon atoms. The bond energy of the covalent C—F bond reaches 546 kJ/mol [40], indicating that when exposed to aqueous electrolytes, dissolution of F atoms into the electrolyte is prevented, thereby mitigating corrosion of electrodes and current collectors for long-term stable cycling performance of zinc anodes in aqueous electrochemical systems. Furthermore, since F atoms have the highest electronegativity among all elements, FGNSs as coating materials are expected to impart good hydrophobicity to zinc anodes.

The morphology of the coated zinc metal anode is shown in Fig. 3. Thanks to the nanosheet structure resembling graphite, the fully stirred coating slurry exhibits a remarkably fine texture, enabling effortless and uniform coverage of the commercial zinc foil surface using a spatula. The dried coated anode presents a smooth surface without any indication of bulging or cracking. Under optical microscope (Fig. 3(a)), the coating surface displays excellent uniformity. Further examination through SEM reveals intricate porous and granular microstructure with numerous pore structures (Fig. 3(b)). The cross-sectional SEM image (Fig. 3(c)) shows that the coating thickness is approximately 14 μm, which is comparable to other reported coating materials. Moreover, the entire coating unveils interconnected pore structures, extending into contact with the zinc metal substrate. These pore structures are expected to enhance dispersed mass transfer of Zn^{2+} during electroplating by providing multiple evenly distributed nucleation sites while simultaneously restricting lateral mass transfer and preventing dendrite growth resulting from aggregated electrodeposition.

The contact angle between the electrolyte and the anode surface serves as a direct indicator of the wettability of the electrolyte on the anode surface. As depicted in Figs. 3(d, e), the contact angles of

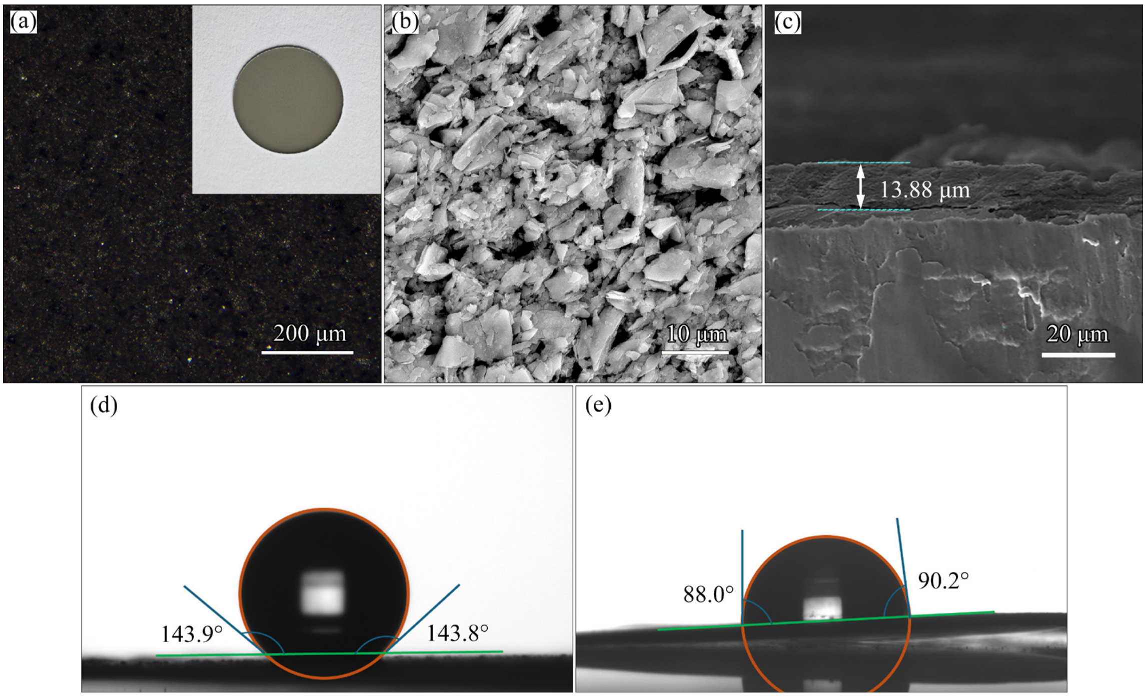

Fig. 3 Photo and optical microscope image of Zn@FGNSs (a); SEM surface (b) and cross-sectional (c) morphology images of Zn@FGNSs; Contact angles of 2 mol/L $ZnSO_4$ aqueous solution on Zn@FGNSs (d), and bare Zn (e)

2 mol/L $ZnSO_4$ aqueous electrolyte on Zn@FGNSs and bare zinc are presented. The untreated commercial zinc foil exhibits an approximate contact angle of 90°, whereas Zn@FGNSs demonstrate significantly higher contact angles, reaching approximately 144°, which closely approaches the standard for superhydrophobic materials. This observation suggests that this coating possesses robust hydrophobic properties. Due to the highest electronegativity of F atoms, the covalent C—F bond exhibits a significant electron pair bias towards the F atom, resulting in a pronounced negative electrical polarity of F atoms. The repulsion among these negatively charged F atoms leads to their exposure on the material surface, forming a protective shell with negative charge. This electrostatic repulsion effectively hinders nucleophilic H_2O from adhering to the coating surface. Such characteristics are advantageous for achieving long-term stable plating/stripping of zinc metal anodes. Considering the corrosion mechanism of zinc anodes in aqueous electrolytes, the majority of corrosion and side reactions are closely associated with H_2O. The hydrophobic interface can effectively mitigate these adverse effects by minimizing the competitive reduction between H^+ (resulting from water ionization) and Zn^{2+}, thereby alleviating hydrogen corrosion and related other side reactions, while simultaneously creating a favorable environment for uniform plating. Moreover, this negatively charged protective layer can exert electrostatic attraction on Zn^{2+}, reducing lateral mass transfer and preventing excessive localized deposition of Zn^{2+}, thus inhibiting uncontrolled dendrite growth.

3.2 Electrochemical performance of Cu@FGNSs symmetrical cells

The coulombic efficiency, which indicates the reversibility of zinc plating/stripping, is defined as the ratio of the amount of zinc that dissolves and deposits during each cycle. A half-cell was assembled using a copper foil coated with FGNSs as the working electrode, while a commercial zinc foil served as the counter electrode. Discharge was conducted at a current density of 5 mA/cm to deposit zinc onto the copper foil, with a deposition capacity of 1 mA·h/cm. Subsequently, the cell was charged to 0.5 V to ensure complete stripping of deposited zinc from the copper foil. The test results are shown in Fig. 4. The Cu||Bare Zn half-cell with FGNSs coating demonstrates exceptional stability, maintaining a nearly constant coulombic efficiency close to 100% for over 1400 cycles (Fig. 4(a)). In contrast, the Cu||Bare Zn half-cell exhibits an unstable coulombic efficiency significantly below 100%, with pronounced oscillations after approximately 250 cycles, indicating a substantial decline in the reversibility of plating/stripping. Consequently, this results in a short circuit within 400 cycles. The voltage−capacity curves corresponding to different cycle counts are presented in Figs. 4(b, c). The Cu@FGNSs||Bare Zn cell consistently displays highly reproducible voltage−capacity curves across various cycle counts. However, the control cell exhibits fluctuations in stripping capacity due to the formation of irreversible “dead zinc” resulting from corrosion and side reactions. Furthermore, the overpotential between the deposition and stripping curves can partially reflect the kinetic performance of Zn^{2+} at the interface. Notably, Cu@FGNSs||Bare Zn cell demonstrates a significantly lower overpotential (~59.2 mV) compared to that of the untreated Cu||Bare Zn cell (~104.8 mV), indicating excellent ion transport kinetics and reduced plating/stripping overpotential under the FGNSs coating.

Galvanostatic cycling tests of Zn@FGNSs||Zn@FGNSs and Bare Zn||Bare Zn symmetrical cells are shown in Fig. 5. Initially, the rate performance of the symmetrical cells was evaluated to assess the overall kinetic performance by comparing the deposition overpotential at different current densities, as shown in Fig. 5(a). The Zn@FGNSs||Zn@FGNSs cell consistently exhibits a lower deposition overpotential than the Bare Zn||Bare Zn cell, indicating improved Zn^{2+} transport kinetics with the FGNSs coating. To assess the long-term stability of the Zn@FGNSs electrodes during repeated plating/stripping, galvanostatic cycling tests were conducted at various current densities. The results demonstrate that with protection and regulation provided by the FGNSs coating, reversibility of zinc metal anode is significantly enhanced. Under a current density of 1 mA/cm with a deposition capacity of 1 mA·h/cm^2, the Zn@FGNSs||Zn@FGNSs symmetrical cell can maintain a fairly consistent overpotential for over 1000 h of reversible plating/stripping (Fig. 5(b)).

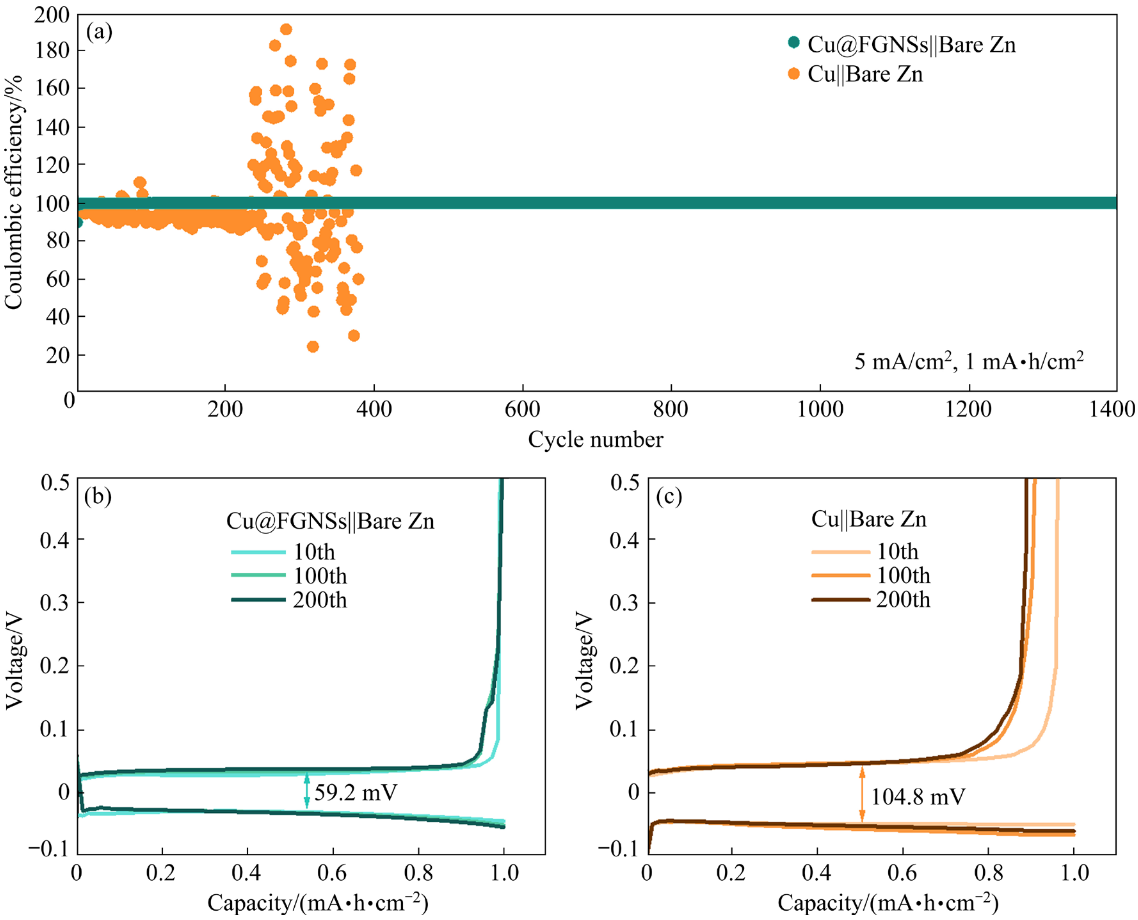

Fig. 4 Coulombic efficiency of Cu@FGNSs||Bare Zn and Cu||Bare Zn cells (a); Voltage−capacity plots of Cu@FGNSs||Bare Zn (b) and Cu||Bare Zn cells (c)

This represents a significant improvement compared to the Bare Zn||Bare Zn symmetrical cell, which encounters a short circuit after approximately 190 h due to a sharp drop in deposition potential, indicating penetration of dendrites through the separator and causing the short circuit. In further experiments, the long-cycle performance of both cells at 5 mA/cm^2, 1 mA·h/cm^2 and 10 mA/cm^2, 2 mA·h/cm^2 was tested. The Zn@FGNSs||Zn@FGNSs symmetrical cells consistently exhibit notable advantages under these more demanding test conditions, achieving stable cycling for durations of 1400 and 400 h, respectively, both outperforming the Bare Zn||Bare Zn symmetrical cell (Figs. 5(c, d)). The latter experiences short-circuit failure after approximately 530 and 150 h during plating/stripping cycles along with a continuous increase in deposition overpotential. This observation suggests that internal dendrite growth and accumulation of byproducts creat an escalating barrier for Zn^{2+} deposition, leading to deteriorating plating conditions.

3.3 Effect of FGNSs coating

To more intuitively compare the effect of FGNSs on suppressing dendrite growth, electrodes from symmetrical cells after plating/stripping for 50 cycles at 5 mA/cm^2, 1 mA·h/cm^2 were disassembled and their surface and cross-sectional morphologies were examined using SEM, as shown in Figs. 6(a−d). After plating/stripping cycles, the FGNSs coating on Zn@FGNSs anode (Fig. 6(a)) largely retains its original appearance, maintaining a porous granular morphology without cracks or detachment. The deposited zinc metal grows beneath the coating without any observable dendrites piercing through it. In contrast, the bare zinc surface (Fig. 6(b)) is covered with dendrites and protrusions resulting from uneven zinc deposition. The cross-sectional analysis further accentuates these differences. The cross-section image of Zn@FGNSs electrode (Fig. 6(c)) clearly displays an intact FGNSs coating along with a uniform and smooth layer of deposited zinc underneath it. Conversely, in the cross-section image

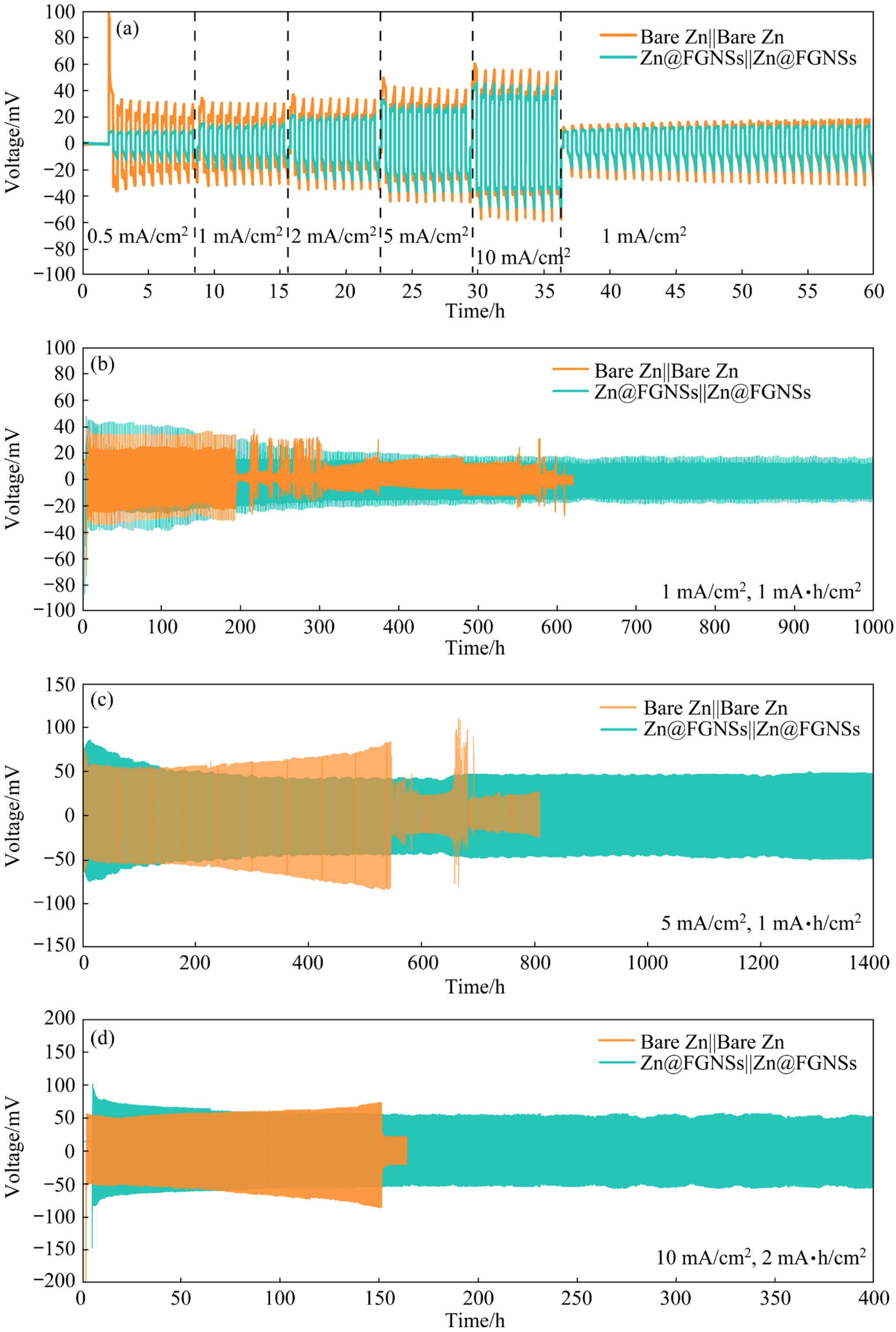

Fig. 5 Rate performance of symmetric cells with Zn@FGNSs and bare Zn from 0.5 to 10 mA/cm^2 (a); Galvanostatic voltage profiles for Zn@FGNSs||Zn@FGNSs and Bare Zn||Bare Zn symmetric cells at 1 mA/cm^2, 1 mA·h/cm^2 (b), 5 mA/cm^2, 1 mA·h/cm^2 (c) and 10 mA/cm^2, 2 mA·h/cm^2 (d)

of the bare zinc electrode (Fig. 6(d)), chaos prevail with noticeable sharp dendrites and granular by-products present. Additionally, many glass fibers are entangled with dendrites, making it difficult to remove them cleanly. These findings suggest that the porous structure provided by FGNSs restricts Zn^{2+} from forming non-uniform flux on the anode surface while promoting nucleation at multiple points to maintain a consistent and smooth layer during zinc plating process. Additionally, due to its hydrophobic nature, this coating effectively isolates a significant number of H_2O molecules from direct interaction with the metal substrate, thereby reducing hydrogen evolution corrosion as well as side reactions.

The chronoamperometry (CA) curves for Zn@FGNSs and bare zinc anode were tested by applying a potential of −200 mV, as shown in Fig. 7(a). When the potential is applied to the bare zinc electrode, the current density continues to

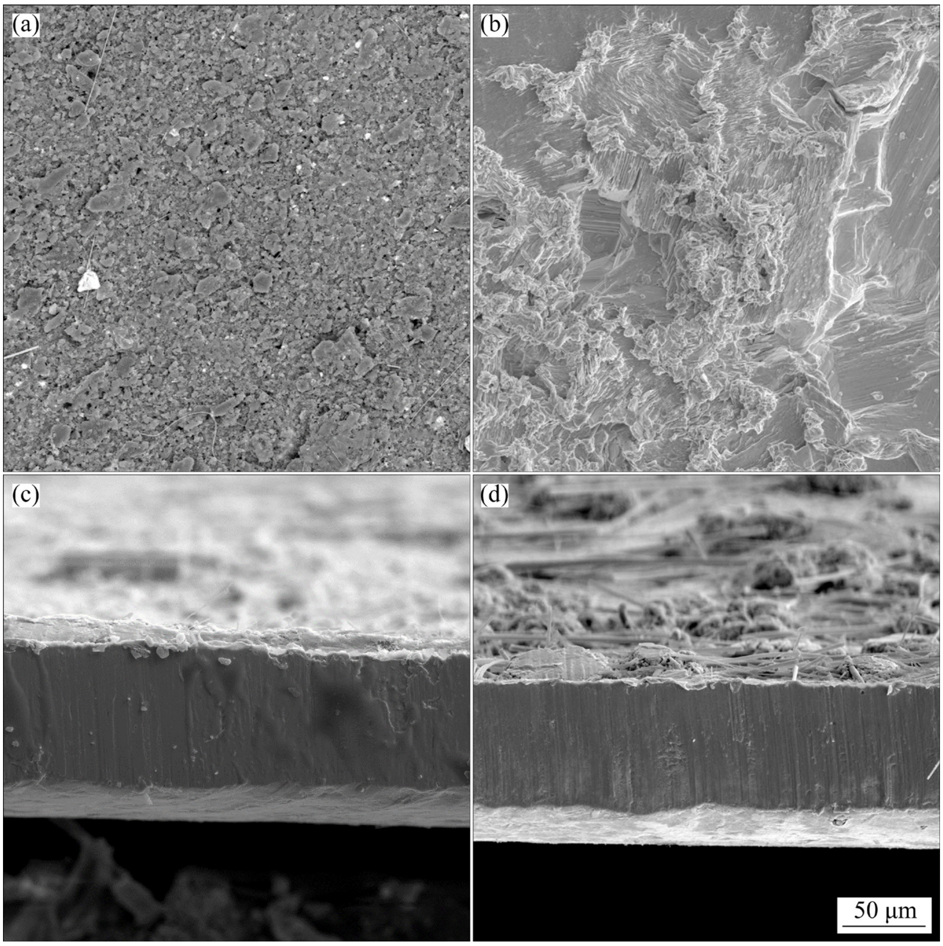

Fig. 6 Surface SEM images of Zn@FGNSs (a), and bare Zn (b) electrodes after 50 plating/stripping cycles; Cross-sectional SEM images of Zn@FGNSs (c), and bare Zn (d) electrodes after 50 plating/stripping cycles in symmetric cells

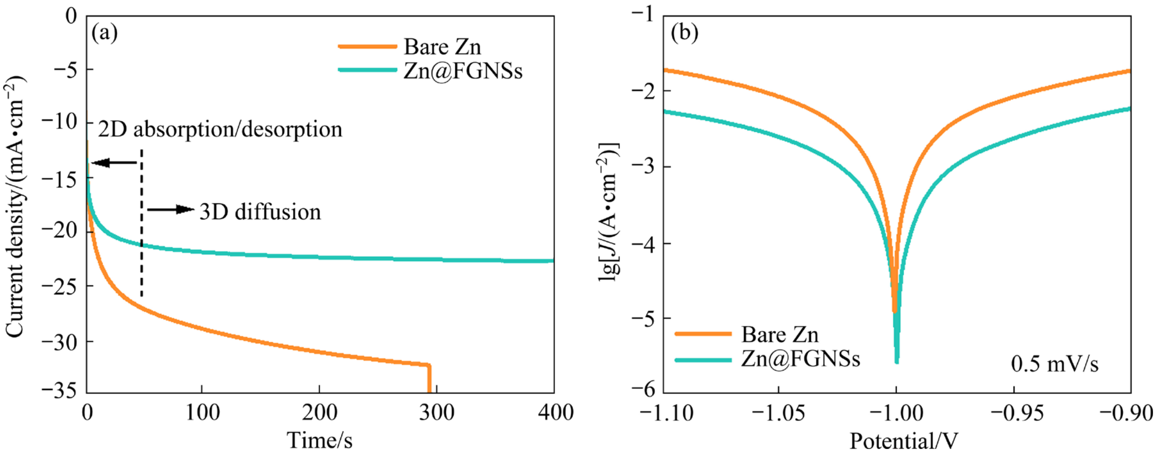

Fig. 7 Chronoamperometry (CA) curves of Zn@FGNSs and bare Zn at constant potential of −200 mV (a); Linear polarization curves generated for Zn@FGNSs and bare Zn (b)

increase even after 200 s, indicating a sustained and widespread 2D diffusion process at the interface between the electrolyte and the anode, resulting in rough deposition growth. To minimize surface energy and exposed area, Zn^{2+} tends to deposit at sites with smaller radii of curvature. If lateral diffusion is not limited, Zn^{2+} adsorbed on the electrode surface can continue to diffuse laterally, seeking energetically favorable locations for charge transfer, eventually leading to aggregation and the formation of dendritic structures. In contrast, the initial nucleation and 2D diffusion process for zinc on Zn@FGNSs electrode basically end within 50 s, after which the current density tends to stabilize, indicating the start of a stable and continuous 3D diffusion process, which suggests that the 2D diffusion of adsorbed Zn^{2+} is limited. The FGNSs coating adhering to the zinc metal substrate provides an additional energy barrier for adsorbed Zn^{2+}, impeding lateral diffusion. Consequently, these Zn^{2+} are compelled to deposit near their initial adsorption points. The dense pore structure of the coating ensures an even distribution of nucleation sites, and with smaller nucleation seeds and higher density, the plating process eventually evolves into a uniform and compact metal layer.

The hydrogen evolution corrosion and accumulation of byproducts on zinc metal anodes during operation significantly impact the cycling stability of battery systems. Since the by-products primarily consist of insoluble basic zinc sulfate salts, their deposition on the metal anode surface reduces the number of available nucleation sites, resulting in increased polarization and dendrite growth. To assess the protective effect of the coating, linear polarization curves were measured for Zn@FGNSs and bare zinc electrodes (Fig. 7(b)), with corrosion current and corrosion potential calculated based on the Tafel equation. Although there is a slight positive shift in corrosion potential for Zn@FGNSs compared to bare zinc, it is negligible. However, the corrosion current for Zn@FGNSs (0.939 mA/cm^2) is significantly lower than that for the bare zinc electrode (3.371 mA/cm^2). Given the same corrosion potential, the reduction in corrosion current indicates that under the protection of the FGNSs coating, the rate of hydrogen evolution corrosion and side reactions on the zinc metal anode is reduced, demonstrating an improvement in corrosion resistance.

3.4 Electrochemical performance of Zn@FGNSs in combination with $NH_4V_4O_{10}$ electrodes

To evaluate the electrochemical performance of Zn@FGNSs anode in full cells, $NH_4V_4O_{10}$ was used as the cathode material and paired with metal anodes. Galvanostatic cycling tests were conducted for both and $NH_4V_4O_{10}$||Bare Zn full cells at different current densities (Figs. 8(a, b)). The cell

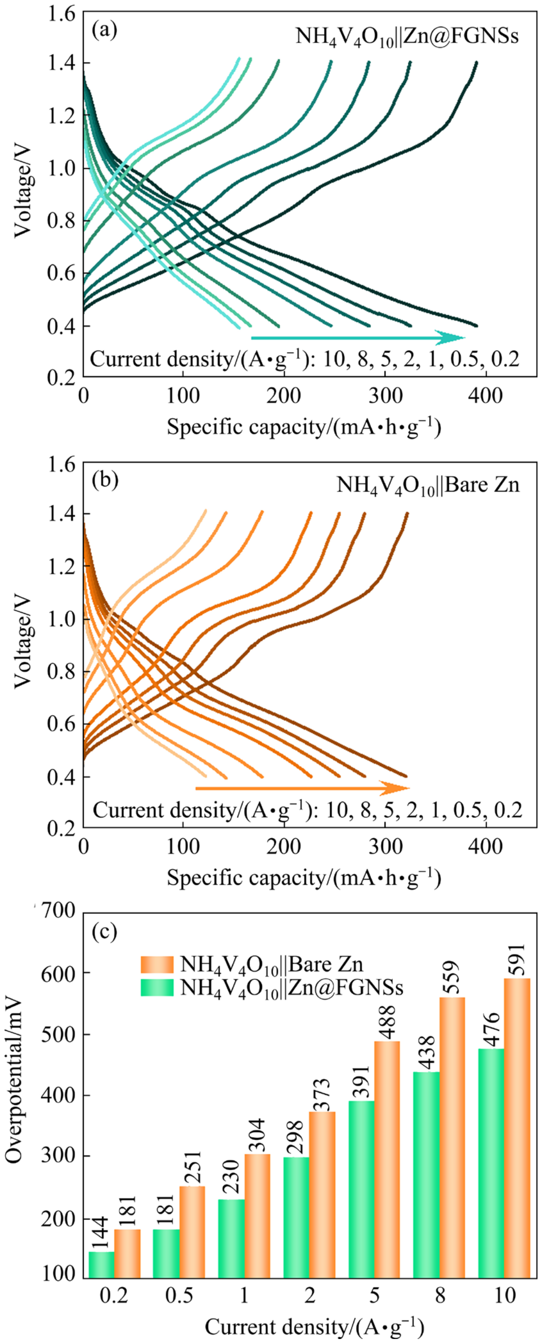

Fig. 8 Electrochemical performance of $NH_4V_4O_{10}$|| Zn@FGNSs and $NH_4V_4O_{10}$||Bare Zn full cells: (a, b) Galvanostatic charge−discharge profiles at various current densities; (c) Corresponding overpotential−current density comparison

exhibits higher specific capacities across various current densities due to the high reactivity and low polarization of the Zn@FGNSs electrode. At a current density of 0.2 A/g, the cell delivers a specific capacity of 389.5 mA·h/g. Additionally, Fig. 8(c) shows that the voltage hysteresis for both cells at different current densities is lower in the $NH_4V_4O_{10}$||Zn@FGNSs cell compared to bare Zn cell, particularly at higher current densities, indicating stable and rapid transport kinetics of Zn^{2+} deposition on Zn@FGNSs anode.

The rate cycling performance of full cells is shown in Fig. 9(a), where $NH_4V_4O_{10}$||Zn@FGNSs cell exhibits superior rate performance, achieving a specific capacity of 191.2 mA·h/g at 10 A/g, surpassing that of $NH_4V_4O_{10}$||Bare Zn cell. The long-cycle performance at constant current is shown in Fig. 9(b), where a current density of 5 A/g, appropriate for $NH_4V_4O_{10}$ cathode, was chosen to evaluate the long-term cycling stability of metal anode. The $NH_4V_4O_{10}$||Zn@FGNSs cell demonstrates an initial specific capacity of 230.6 mA·h/g, and maintains a specific capacity of 212.5 mA·h/g after undergoing 1000 cycles with a remarkable capacity retention rate of 92.2%. In contrast, $NH_4V_4O_{10}$||Bare Zn cell exhibits inferior cycling stability significantly as its specific capacity declines from 215.3 to only 134.2 mA·h/g resulting in a mere capacity retention rate of 62.3%. The CV curves for $NH_4V_4O_{10}$||Zn@FGNSs and $NH_4V_4O_{10}$||Bare Zn cells are shown in Fig. 10(a). The $NH_4V_4O_{10}$||Zn@FGNSs cell exhibits a higher current density compared to the control group, indicating superior electrochemical reactivity of Zn@FGNSs anode over bare zinc. Furthermore, the EIS spectra for both full cells are depicted in Fig. 10(b). Notably, Zn@FGNSs demonstrates lower charge transfer resistance than bare zinc, which remains consistent even after undergoing 50 cycles at a current density of 5 A/g.

4 Conclusions

(1) The coating exhibits a compact porous structure that effectively promotes uniform electrolyte flux at the interface during electrochemical reactions. This physical constraint restricts lateral mass transfer of Zn^{2+} while providing numerous evenly distributed nucleation sites for zinc plating.

(2) Due to the high electronegativity of fluorine atoms, a negatively charged protective layer

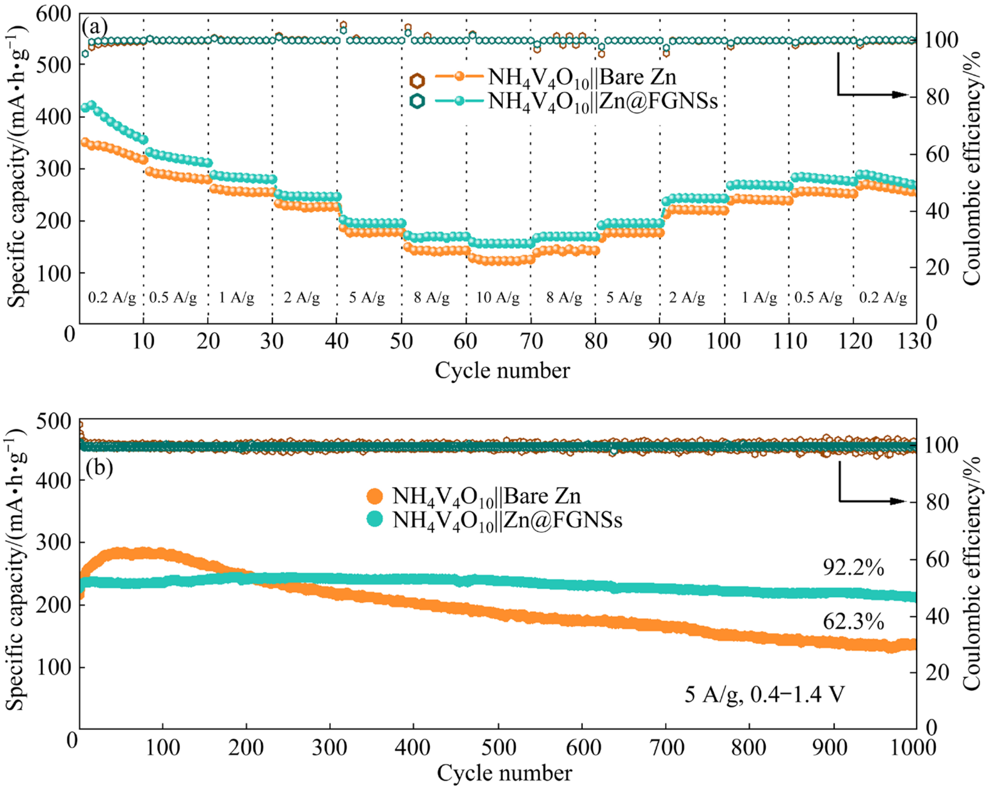

Fig. 9 Rate performance (a), cycling performance and coulombic efficiency (b) of $NH_4V_4O_{10}$||Zn@FGNSs and $NH_4V_4O_{10}$||Bare Zn full cells

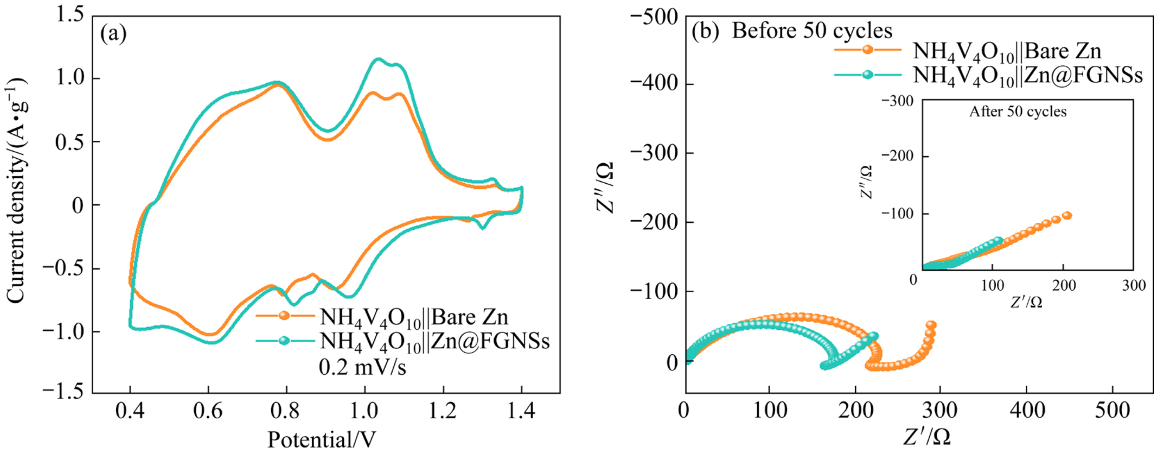

Fig. 10 CV plots (a) and Nyquist plots (b) of $NH_4V_4O_{10}$||Zn@FGNSs and $NH_4V_4O_{10}$||Bare Zn full cells

is formed on the surface of the material, leading to the development of a nearly super- hydrophobic surface that repels solvent H_2O. Consequently, this suppresses hydrogen evolution corrosion and related side reactions.

(3) Remarkable stability is observed in symmetric cells, maintaining reversible charge−discharge processes for over 1400 h at a current density of 5 mA/cm^2. Furthermore, excellent electrochemical performance is demonstrated in full cells. Specifically, the $NH_4V_4O_{10}$||Zn@FGNSs cell achieves an impressive specific capacity of 212.5 mA·h/g with a capacity retention rate of 92.2% after undergoing 1000 cycles.

CRediT authorship contribution statement

Hong CHANG: Writing − Original draft, Visualization, Investigation, Formal analysis, Data curation; **Zhen-ya LUO:** Resources, Methodology; **Xue-ru SHI:** Visualization, Software; **Xin-xin CAO:** Writing − Review & editing, Supervision, Project administration, Funding acquisition, Conceptualization; **Shu-quan LIANG:** Resources, Project administration.

Declaration of competing interest

The authors declare that they have no known competing financial interests or personal relationships that could have appeared to influence the work reported in this paper.

Acknowledgments

This work was supported by Young Elite Scientists Sponsorship Program by CAST, China (No. 2023QNRC001), the Science and Technology Innovation Program of Hunan Province, China (No. 2022RC1078), the Natural Science Foundation of Hunan Province, China (No. 2023JJ10060), and the Scientific Research Fund of Hunan Provincial Education Department, China (No. 23A0003).

References

[1] WANG Jin, LI Yu-shan, LIU Peng, WANG Feng, YAO Qing-rong, ZOU Yong-jin, ZHOU Huai-ying, BALOGUN M S, DENG Jian-qiu. Green large-scale production of N/O-dual doping hard carbon derived from bagasse as high-performance anodes for sodium-ion batteries [J]. Journal of Central South University, 2021, 28(2): 361−369.

[2] SU Qiong, ZHOU Yi-fan, ZHU Jue, CHANG Hong, HOU Min, CAO Xin-xin, LIANG Shu-quan. Nanoflake-assembled hierarchical $Na_3V_2(PO_4)_3$@C microspheres for ultrafast and highly durable sodium storage [J]. ACS Applied Energy Materials, 2023, 6(19): 10128−10136.

[3] CHANG Yi-jiao, XIE Guang-hui, ZHOU Yong-mao, WANG Jie-xi, WANG Zhi-xing, GUO Hua-jun, YOU Bian-zheng, YAN Guo-chun. Enhancing storage performance of P2-type $Na_{2/3}Fe_{1/2}Mn_{1/2}O_2$ cathode materials by Al_2O_3 coating [J]. Transactions of Nonferrous Metals Society of China, 2022, 32(1): 262−272.

[4] QIN Mu-lan, YIN Chang-yu, XU Wen, LIU Yang, WEN Jun-hao, SHEN Bin, WANG Wei-gang, LIU Wan-min. Facile synthesis of high capacity P2-type $N_{a2/3}Fe_{1/2}Mn_{1/2}O_2$ cathode material for sodium-ion batteries [J]. Transactions of Nonferrous Metals Society of China, 2021, 31(7): 2074−2080.

[5] ZHANG Wen, LIU Ye, YE Zhong-qiang, YANG Min, LUO Qi, DAI Jing, WANG Qian-fu, LIU Li. Porous nitrogen-doped FeP/C nanofibers as promising anode for potassium-ion batteries [J]. Journal of Central South University, 2023, 30(10): 3248−3259.

[6] OU Hui-huang, HUANG Ji-wu, ZHOU Yi-fan, ZHU Jue, FANG Guo-zhao, CAO Xin-xin, LI Jiang-xu, LIANG Shu-quan. Surface-dominated ultra-stable sodium and potassium storage enabled by N/P/O tri-doped porous carbon [J]. Chemical Engineering Journal, 2022, 450: 138444.

[7] LIU Zhen, HE Han-bing, LUO Ze-xiang, WANG Xiao-feng,

ZENG Jing. 3D printing of customized MnO_2 cathode for aqueous zinc-ion batteries [J]. Transactions of Nonferrous Metals Society of China, 2023, 33(4): 1193−1204.

[8] WANG Ting-ting, LI Can-peng, XIE Xue-song, LU Bing-an, HE Zhang-xing, LIANG Shu-quan, ZHOU Jiang. Anode materials for aqueous zinc ion batteries: Mechanisms, properties, and perspectives [J]. ACS Nano, 2020, 14(12): 16321−16347.

[9] NIE Wei, CHENG Hong-wei, SUN Qiang-chao, LIANG Shu-quan, LU Xiong-gang, LU Bing-an, ZHOU Jiang. Design strategies toward high-performance Zn metal anode [J]. Small Methods, 2024, 8(6): 2201572.

[10] LI Bin, ZHANG Xiao-tan, WANG Ting-ting, HE Zhang-xing, LU Bing-an, LIANG Shu-quan, ZHOU Jiang. Interfacial engineering strategy for high-performance Zn metal anodes [J]. Nano-Micro Letters, 2022, 14: 1−31.

[11] LI Can-peng, XIE Xue-song, LIANG Shu-quan, ZHOU Jiang. Issues and future perspective on zinc metal anode for rechargeable aqueous zinc-ion batteries [J]. Energy & Environmental Materials, 2020, 3(2): 146−159.

[12] YANG Qi, LI Qing, LIU Zhuo-xin, WANG Dong-hong, GUO Ying, LI Xin-liang, TANG Yong-chao, LI Hong-fei, DONG Bin-bin, ZHI Chun-yi. Dendrites in Zn-based batteries [J]. Advanced Materials, 2020, 32(48): 2001854.

[13] ZUO Ya-yu, WANG Ke-liang, PEI Pu-cheng, WEI Man-hui, LIU Xiao-tian, XIAO Yu, ZHANG Peng-fei. Zinc dendrite growth and inhibition strategies [J]. Materials Today Energy, 2021, 20: 100692.

[14] ZENG Xiao-hui, XIE Kai-xuan, LIU Sai-lin, ZHANG Shi-lin, HAO Jun-nan, LIU Jia-tu, PANG Wei-kong, LIU Jian-wen, RAO Pin-hua, WANG Qing-hong, MAO Jian-feng, GUO Zai-ping. Bio-inspired design of an in situ multifunctional polymeric solid-electrolyte interphase for Zn metal anode cycling at 30 $mA\cdot cm^{-2}$ and 30 $mA\cdot h\cdot cm^{-2}$ [J]. Energy & Environmental Science, 2021, 14(11): 5947−5957.

[15] CAI Zhao, WANG Jin-di, SUN Yong-ming. Anode corrosion in aqueous Zn metal batteries [J]. eScience, 2023, 3(1): 100093.

[16] CAI Zhao, OU-YANG Tao, WANG Jin-di, XIAO Run, FU Lin, YUAN Zhu, ZHAN Ren-min, SUN Yong-ming. Chemically resistant Cu−Zn/Zn composite anode for long cycling aqueous batteries [J]. Energy Storage Materials, 2020, 27: 205−211.

[17] ZHAO Jing-wen, ZHANG Jian, YANG Wu-hai, CHEN Bing-bing, ZHAO Zhi-ming, QIU Hua-yu, DONG Shan-mu, ZHOU Xin-hong, CUI Guang-lei, CHEN Li-quan. “Water-in-deep eutectic solvent” electrolytes enable zinc metal anodes for rechargeable aqueous batteries [J]. Nano Energy, 2019, 57: 625−634.

[18] TANG Yan, LIU Cun-xin, ZHU Han-rui, XIE Xue-song, GAO Jia-wei, DENG Can-bin, HAN Ming-ming, LIANG Shu-quan, ZHOU Jiang. Ion-confinement effect enabled by gel electrolyte for highly reversible dendrite-free zinc metal anode [J]. Energy Storage Materials, 2020, 27: 109−116.

[19] DING Yi-qing, ZHANG Xiao-tan, WANG Tian-qi, LU Bing-an, ZENG Zhi-yuan, TANG Yan, ZHOU Jiang, LIANG Shu-quan. A dynamic electrostatic shielding layer toward highly reversible Zn metal anode [J]. Energy Storage Materials, 2023, 62: 102949.

[20] HUANG Jing, PENG Qian, LIU Kun, FANG Guo-zhao. Silica-based electrolyte regulation for stable aqueous zinc-manganese batteries [J]. Journal of Central South University, 2023, 30(2): 434−442.

[21] ZHANG Xiao-tan, LI Jiang-xu, QI Kai-wen, YANG Yong-qiang, LIU Dong-yan, WANG Tian-qi, LIANG Shu-quan, LU Bing-an, ZHU Yong-chun, ZHOU Jiang. An ion-sieving janus separator toward planar electrodeposition for deeply rechargeable Zn-metal anodes [J]. Advanced Materials, 2022, 34(38): 2205175.

[22] RUAN Peng-chao, CHEN Xian-hong, QIN Li-ping, TANG Yan, LU Bing-an, ZENG Zhi-yuan, LIANG Shu-quan, ZHOU Jiang. Achieving highly proton-resistant Zn−Pb anode through low hydrogen affinity and strong bonding for long-life electrolytic Zn//MnO_2 battery [J]. Advanced Materials, 2023, 35(31): 2300577.

[23] ZHOU Miao, GUO Shan, LI Jia-lin, LUO Xiong-bin, LIU Zhe-xuan, ZHANG Teng-sheng, CAO Xin-xin, LONG Meng-qiu, LU Bing-an, PAN An-qiang, FANG Guo-zhao, ZHOU Jiang, LIANG Shu-quan. Surface-preferred crystal plane for a stable and reversible zinc anode [J]. Advanced Materials, 2021, 33(21): 2100187.

[24] WANG Pin-ji, LIANG Shu-quan, CHEN Chen, XIE Xue-song, CHEN Jia-wen, LIU Zhen-han, TANG Yan, LU Bing-an, ZHOU Jiang. Spontaneous construction of nucleophilic carbonyl-containing interphase toward ultrastable zinc-metal anodes [J]. Advanced Materials, 2022, 34(33): 2202733.

[25] WANG Ting-ting, WANG Pin-ji, PAN Liang, HE Zhang-xing, DAI Lei, WANG Ling, LIU Shu-de, JUN S C, LU Bing-an, LIANG Shu-quan, ZHOU Jiang. Stabling zinc metal anode with polydopamine regulation through dual effects of fast desolvation and ion confinement [J]. Advanced Energy Materials, 2023, 13(5): 2203523.

[26] WANG Tian-qi, TANG Yan, YU Min-xiao, LU Bing-an, ZHANG Xiao-tan, ZHOU Jiang. Spirally grown zinc-cobalt alloy layer enables highly reversible zinc metal anodes [J]. Advanced Functional Materials, 2023, 33(51): 2306101.

[27] DENG Can-bin, XIE Xue-song, HAN Jun-wei, LU Bing-an, LIANG Shu-quan, ZHOU Jiang. Stabilization of Zn metal anode through surface reconstruction of a cerium-based conversion film [J]. Advanced Functional Materials, 2021, 31(51): 2103227.

[28] ZHOU Shuang, WANG Ya-ping, LU Hao-tian, ZHANG Yi-fang, FU Chun-yan, USMAN Ibrahim, LIU Zhe-xuan, FENG Ming-yang, FANG Guo-zhao, CAO Xin-xin, LIANG Shu-quan, PAN An-qiang. Anti-corrosive and Zn-ion-regulating composite interlayer enabling long-life Zn metal anodes [J]. Advanced Functional Materials, 2021, 31(46): 2104361.

[29] PENG Hai-jun, FANG Yun, WANG Jin-zhe, RUAN Peng-chao, TANG Yan, LU Bing-an, CAO Xin-xin, LIANG Shu-quan, ZHOU Jiang. Constructing fast-ion-conductive disordered interphase for high-performance zinc-ion and zinc-iodine batteries [J]. Matter, 2022, 5(12): 4363−4378.

[30] GAO Yu-meng, LIU Yong, FENG Kai-jia, MA Jun-qing, MIAO Ying-jie, XU Bin-rui, PAN Kun-ming, AKIYOSHI O, WANG Guang-xin, ZHANG Ke-ke, ZHANG Qiao-bao. Emerging WS_2/WSe_2@graphene nanocomposites: Synthesis

and electrochemical energy storage applications [J]. Rare Metals, 2024, 43(1): 1−19.

[31] XIA Ao-lin, PU Xiao-ming, TAO Ya-yuan, LIU Hai-mei, WANG Yong-gang. Graphene oxide spontaneous reduction and self-assembly on the zinc metal surface enabling a dendrite-free anode for long-life zinc rechargeable aqueous batteries [J]. Applied Surface Science, 2019, 481: 852−859.

[32] SHEN Chao, LI Xin, LI Nan, XIE Ke-yu, WANG Jian-gan, LIU Xing-rui, WEI Bing-qing. Graphene-boosted, high-performance aqueous Zn-ion battery [J]. ACS Applied Materials & Interfaces, 2018, 10(30): 25446−25453.

[33] LI Hong-fei, XU Cheng-jun, HAN Cui-ping, CHEN Yan-yi, WEI Chun-guang, LI Bao-hua, KANG Fei-yu. Enhancement on cycle performance of Zn anodes by activated carbon modification for neutral rechargeable zinc ion batteries [J]. Journal of the Electrochemical Society, 2015, 162(8): A1439.

[34] DONG Liu-bing, YANG Wu, YANG Wang, TIAN Hao, HUANG Yong-feng, WANG Xian-li, XU Cheng-jun, WANG Cheng-yin, KANG Fei-yu, WANG Guo-xiu. Flexible and conductive scaffold-stabilized zinc metal anodes for ultralong-life zinc-ion batteries and zinc-ion hybrid capacitors [J]. Chemical Engineering Journal, 2020, 384: 123355.

[35] HAN Da-liang, WU Shi-chao, ZHANG Si-wei, DENG Ya-qian, CUI Chang-jun, ZHANG Li-na, LONG Yu, LI Huan, TAO Ying, WENG Zhe, YANG Quan-hong, KANG Fei-yu. A corrosion-resistant and dendrite-free zinc metal anode in aqueous systems [J]. Small, 2020, 16(29): 2001736.

[36] WANG Xu, WANG Wei-miao, LIU Yang, REN Meng-meng, XIAO Hui-ning, LIU Xiang-yang. Characterization of conformation and locations of C—F bonds in graphene derivative by polarized ATR-FTIR [J]. Analytical chemistry, 2016, 88(7): 3926−3934.

[37] LI Bao-yin, HE Tai-jun, WANG Zao-ming, CHENG Zheng, LIU Yang, CHEN Teng, LAI Wen-chuan, WANG Xu, LIU Xiang-yang. Chemical reactivity of C—F bonds attached to graphene with diamines depending on their nature and location [J]. Physical Chemistry Chemical Physics, 2016, 18(26): 17495−17505.

[38] ZHU Yan-lei, ZHANG Li-juan, ZHAO Hui-hui, FU Yu. Significantly improved electrochemical performance of CF_x promoted by SiO_2 modification for primary lithium batteries [J]. Journal of Materials Chemistry A, 2017, 5(2): 796−803.

[39] TRESSAUD A, MOGUET F, FLANDROIS S, CHAMBON M, GUIMON C, NANSE G, PAPIRER E, GUPTA V, BAHL OP. On the nature of C—F bonds in various fluorinated carbon materials: XPS and TEM investigations [J]. Journal of Physics and Chemistry of Solids, 1996, 57(6/7/8): 745−751.

[40] LEMAL D M. Perspective on fluorocarbon chemistry [J]. The Journal of Organic Chemistry, 2004, 69(1): 1−11.

稳定可逆的氟化石墨纳米片涂层锌金属负极

常 鸿[1]，罗振亚[2]，石雪茹[1]，曹鑫鑫[1]，梁叔全[1]

1. 中南大学 材料科学与工程学院 电子封装及先进功能材料湖南省重点实验室，长沙 410083；
2. 湘潭大学 材料科学与工程学院，湘潭 411105

摘　要：设计了一种采用氟化石墨纳米片涂层改性的高稳定锌金属负极。涂层具有多孔结构，阻止锌离子横向传质，并抑制枝晶生长；氟原子的高电负性形成近乎超疏水的固液界面，减少溶剂水与锌基体之间的相互作用，抑制析氢腐蚀和其他副反应。涂层负极表现出优异的循环稳定性，对称电池在电流密度 5 mA/cm²条件下稳定循环超过 1400 h；使用 $NH_4V_4O_{10}$ 正极的全电池在循环 1000 次后容量保持率为 92.2%。

关键词：氟化石墨；疏水涂层；抗腐蚀；枝晶抑制；锌金属负极

(Edited by Bing YANG)